

# Group IV Mid-Infrared Thermophotovoltaic Cells on Silicon

G erard Daligou,<sup>1</sup> Richard Soref,<sup>2</sup> Anis Attiaoui,<sup>1</sup> Jaker Hossain,<sup>3</sup> Mahmoud R. M. Atalla,<sup>1</sup> Patrick Del Vecchio,<sup>1</sup> and Oussama Moutanabbir<sup>1,\*</sup>

<sup>1</sup>*Department of Engineering Physics,  cole Polytechnique de Montr al, C.P. 6079, Succ. Centre-Ville, Montr al, Qu bec, Canada H3C 3A7*

<sup>2</sup>*Department of Engineering, University of Massachusetts Boston, Boston, MA 02125, USA*

<sup>3</sup>*Solar Energy Laboratory, University of Rajshahi 6205, Bangladesh*

Compound semiconductors have been the predominant building blocks for the current mid-infrared thermophotovoltaic devices relevant to sub-2000 K heat conversion and power beaming. However, the prohibitively high cost associated with these technologies limits their broad adoption. Herein, to alleviate this challenge we introduce an all-group IV mid-infrared cell consisting of GeSn alloy directly on a silicon wafer. This emerging class of semiconductors provides strain and composition as degrees of freedom to control the bandgap energy thus covering the entire mid-infrared range. The proposed thermophotovoltaic device is composed of a fully relaxed Ge<sub>0.83</sub>Sn<sub>0.17</sub> double heterostructure corresponding to a bandgap energy of 0.29 eV. A theoretical framework is derived to evaluate cell performance under high injection. The black-body radiation absorption is investigated using the generalized transfer matrix method thereby considering the mixed coherent/incoherent layer stacking. Moreover, the intrinsic recombination mechanisms and their importance in a narrow bandgap semiconductor were also taken into account. In this regard, the parabolic band approximation and Fermi's golden rule were combined for an accurate estimation of the radiative recombination rate. Based on these analyses, power conversion efficiencies of up to 9% are predicted for Ge<sub>0.83</sub>Sn<sub>0.17</sub> thermophotovoltaic cells under black-body radiation at temperatures in the 500-1500 K range. A slight improvement in the efficiency is observed under the frontside illumination but vanishes below 800 K, while the use of a backside reflector improves the efficiency across the investigated black-body temperature range. The effects of the heterostructure thickness, surface recombination velocity, and carrier lifetime are also elucidated and discussed.

## I. INTRODUCTION

Narrow bandgap thermo-photovoltaic (TPV) cells have been the subject of extensive investigations motivated by their strategic importance in harvesting infrared radiations for heat waste conversion, portable devices, power beaming, and space applications [1–5]. In general, TPV cells are electronic devices consisting of a heat generator, a radiator to translate heat into an emission spectrum, an optical filter such as glass or quartz tubes, and a cell that converts infrared photon energy to electrical energy. Recently, tremendous efforts have been expended to develop mid-infrared TPV cells to leverage their several technological advantages such as the potential to exploit the atmospheric transparency windows for eye-safer energy beaming and the ability to generate energy from the staggering amount of heat wasted by major industrial activities [5]. In fact, as illustrated in the chart displayed in Fig. 1(a), vital manufacturing sectors such as iron, steel, cement, glass, and metallurgy suffer large energy footprints exacerbated by heat losses at temperatures below 2000 K. Efficient absorption and conversion of black-body radiations emitted in this range require semiconductors with bandgap energy ( $E_g$ ) smaller than  $\sim 0.7$  eV. Indeed, by simply examining the black-body radiation power density as a function of temperature, while

neglecting sub-bandgap absorption, one can deduce that about 50.5% of the 1000 K black-body radiation can be absorbed by a semiconductor having a bandgap energy of 0.3 eV. This fraction increases to 75.5% and 86.7% at the temperatures of 1500 K and 2000 K, respectively.

Compound semiconductors have been explored to implement both far-field and near-field sub-2000 K TPV cells reporting a measured efficiency in the 1-11% range, while theory hints to higher values reaching 24% [1, 5, 9–11]. For instance, In<sub>0.20</sub>Ga<sub>0.80</sub>As<sub>0.18</sub>Sb<sub>0.82</sub> ( $E_g = 0.5$  eV) TPV cells on lattice-matched GaSb deliver an open circuit voltage ( $V_{OC}$ ) of  $\sim 0.3$  V, a short circuit current density ( $J_{SC}$ ) up to 3 A/cm<sup>2</sup>, and an internal quantum efficiency (IQE) of  $\sim 90\%$  [1, 12, 13]. GaSb TPV cells have the potential to provide a power conversion efficiency (PCE) of  $\sim 16\%$  and are suitable for heat sources ranging from 1300 to 1500 K. These cells exhibit an IQE above 90% at wavelengths up to 1.8  $\mu$ m [9, 14]. However, the Zn diffusion needed to form the  $p$ -type GaSb emitter hinders the cell performance [15]. For InGaAs ( $E_g = 0.74$  eV) TPV cells, a PCE of 9.2-16.4% was reported for black-body temperature in the 873-1323 K range, but the change in the illumination spectrum was shown to have an important impact on the current conduction mechanisms that dominate the minority charge transport in these cells [16, 17]. Narrower bandgap semiconductors such as InAs ( $E_g = 0.35$  eV) yield higher efficiency TPV cells for lower temperature heat sources ( $< 1250$  K) as more radiated low-energy photons can be absorbed by these semiconductors [1, 18]. In this regard, TPV cells employing an

\* oussama.moutanabbir@polymtl.ca

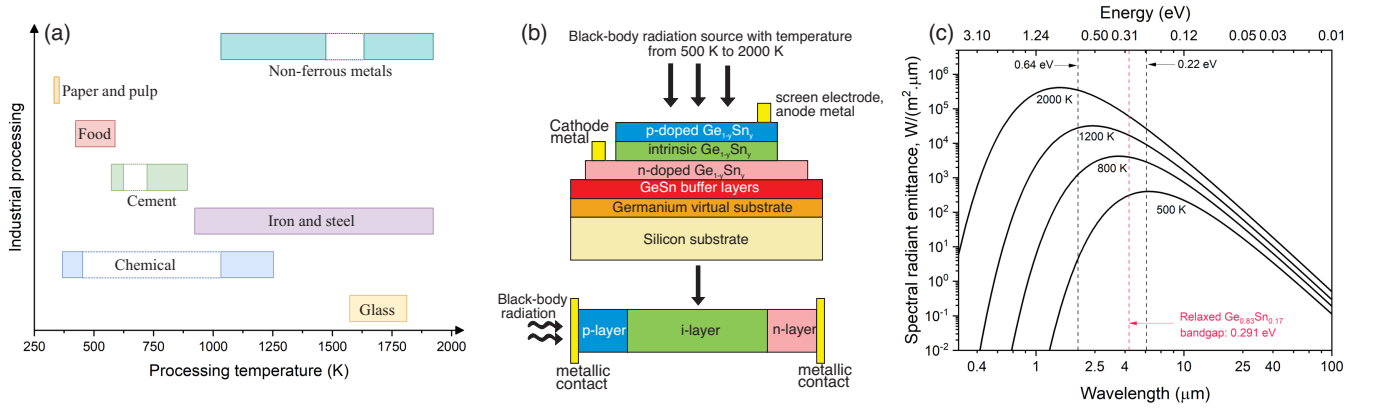


FIG. 1. (a) Processing temperatures used in major manufacturing industries. The data presented in this chart, were mainly extracted from various U.S. Department of Energy reports [6, 7] and [8]. Note that, within the same industry, the temperature range depends on the energy source used to fuel the foundries as well as on the nature of the product developed. For instance, in the industry of non-ferrous metals producing nickel requires a much higher temperature (up to 1923 K) as compared to copper (up to 1363 K) or aluminum (up to 1473 K). (b) Schematic illustration of the Ge<sub>1-y</sub>Sn<sub>y</sub> TPV cell. (c) Evolution of the spectral radiant emittance with wavelength and temperature. The black dashed line indicates the bandgap energy of relaxed Ge<sub>0.95</sub>Sn<sub>0.05</sub> and Ge<sub>0.80</sub>Sn<sub>0.20</sub> semiconductors. At 500 K, assuming no sub-bandgap absorption, only 8.8% of the black body radiation can be absorbed by a relaxed Ge<sub>0.83</sub>Sn<sub>0.17</sub> having bandgap energy of  $\sim 0.29$  eV. This fraction increases to  $\sim 86.7\%$  at 2000 K.

InAs *p-i-n* diode enable a 3.6% PCE at a black-body temperature of 950 °C [1].

Notwithstanding the progress achieved so far in developing narrow bandgap TPV cells, the substrates needed to grow these cells are costly and suffer large dark currents. To mitigate the latter, narrow bandgap interband cascade photovoltaic cells (ICPV) based on InAs/GaSb multiple quantum wells have been recently proposed [19, 20]. These devices alleviate the limiting factors of bulk narrow bandgap TPV (high saturation dark current density, relatively low absorption coefficient, short diffusion length, material quality, etc.) thanks to the type II broken-gap alignment at the InAs/GaSb interface, which mainly enables carrier collection through tunneling. Under standard black-body radiation illumination [19, 20], the ICPV devices operating at 80 K exhibit relatively high  $V_{OC}$  ( $\sim 1.1$  V  $> E_g/e$ ) demonstrating that the multiple stage absorbers operate in series. However, at 300 K the ICPV devices perform poorly with  $V_{OC}$  around 5.7 mV and an output power density below 0.002 mW/cm<sup>2</sup>. The deterioration is attributed to the saturation current density being significantly higher than the photo-current density generated by the radiation from the black-body source.

A cost-effective and scalable alternative to compound semiconductor mid-infrared TPV materials would be the silicon-compatible narrow bandgap Ge<sub>1-y</sub>Sn<sub>y</sub> semiconductors [21]. These group IV alloys are grown on large-diameter silicon wafers and can cover the entire mid-infrared range by increasing the Sn content. Indeed, the recent progress in their epitaxial growth led to the demonstration of a variety of monolithic mid-infrared emitters and detectors [22–38]. Building on these achievements, herein we introduce Ge<sub>1-y</sub>Sn<sub>y</sub> alloys to design silicon-integrated mid-infrared TPV cells and discuss their performance and its evolution as a function of the basic

material properties.

## II. DEVICE STRUCTURE AND THEORETICAL FRAMEWORK

The proposed all-group IV mid-infrared TPV cells consist of a fully relaxed Ge<sub>1-y</sub>Sn<sub>y</sub> *p-i-n* homojunction grown on a silicon wafer using a germanium interlayer - commonly known as a virtual substrate. Fig. 1(b) exhibits a schematic illustration of the device structure. Varying the Sn content between 5 and 20 at.% yields bandgap energies covering the mid-infrared range up to 6  $\mu m$ , as displayed in Fig. 1(c). This composition range is consistent with the recent experimental studies on the growth of Ge<sub>1-y</sub>Sn<sub>y</sub> alloys [21]. Note that the front electrode shadowing and the parasitic resistances are neglected in evaluating the device performance. Moreover, the one-dimensional treatment is justified since the device dimensions are significantly larger than the device thickness. Thus, the performance and the electrical properties of the TPV cell are estimated by solving self-consistently the steady-state coupled Poisson drift-diffusion equations (1):

$$\begin{aligned} \varepsilon_0 \nabla_x (\varepsilon_r \nabla_x \phi) &= -e (p + n + N_D^+ - N_A^-) \\ \nabla_x (\mu_n n \nabla_x E_{f_n}) &= e (R - G) \\ \nabla_x (\mu_p p \nabla_x E_{f_p}) &= -e (R - G) \end{aligned} \quad (1)$$

where  $\varepsilon_r$  is the relative dielectric permittivity,  $\phi$  the electrostatic potential, and  $p + n + N_D^+ - N_A^-$  is the space charge density. Besides  $G - R$  is the net difference between generation and recombination while  $E_{f_n}$  and  $E_{f_p}$  are the electron and holes quasi-Fermi levels, respectively. This set of equations mainly describes the carrier dynamics

and transport, which requires a rigorous description of both the electrical and optical properties of the materials involved. In the simulations of the optical behavior and related calculations of the generation rate  $G(x)$  and the absorbance  $\mathcal{A}$ , the complete stack of layers is considered to describe both the frontside and backside illumination. Once these properties are obtained, as a first approximation, the simulations were restricted to the set of active layers, namely the  $p$ - $i$ - $n$  junction (Fig. 1(b)).

### A. Optical characteristics of the TPV $p$ - $i$ - $n$ device

In a single semiconductor slab, the generation rate  $G(x)$  of electron-hole pairs (EHPs) at a distance  $x$  from the surface is usually derived from the Beer-Lambert law [39, 40]. However, in a multilayered structure with different refractive indices from one layer to the others, light absorption can be significantly affected by the optical interference of the incident and the reflected waves. In this study, the optical transfer matrix method (OTMM) was employed to simulate light propagation through the different layers of the  $\text{Ge}_{1-y}\text{Sn}_y$  TPV cells. For a light incident from the left of the multilayered structure, as shown in Fig. 2, the total electric field in a layer  $j$  at an arbitrary distance  $x$  to the left interface ( $0 \leq x \leq d_j$ , where  $d_j$  is the layer thickness) is given by [41]:

$$E_j(x) = E_j^+(x) + E_j^-(x) \quad (2)$$

The time average of the energy dissipated per second  $Q_j(x, \lambda)$  at a position  $x$  in layer  $j$  and at a specific wavelength  $\lambda$  is given by [41]

$$\begin{aligned} Q_j(x, \lambda) &= \frac{1}{2} c \varepsilon_0 \alpha_j(\lambda) n_j(\lambda) |E_j(x)|^2 \\ &= \left( \frac{\alpha_j n_j}{n_0} \right) |t_j^+|^2 I_0 \left[ e^{-\alpha_j x} + \rho_j'' \cdot e^{\alpha_j (2d_j - x)} \right. \\ &\quad \left. + 2\rho_j'' \cdot e^{-\alpha_j d_j} \cdot \cos \left( \frac{4\pi n_j}{\lambda} (d_j - x) + \delta_j'' \right) \right] \end{aligned} \quad (3)$$

where  $c$  is the speed of light in free space,  $\varepsilon_0$  the vacuum permittivity,  $n_j$  the refractive index of layer  $j$ ,  $n_0$  the refractive index of the ambient environment,  $\alpha_j = 4\pi k_j / \lambda$  the absorption coefficient of layer  $j$ ,  $k_j$  its extinction coefficient,  $I_0 = (hc/\lambda)\phi_f (\frac{hc}{\lambda}, T_{bb})$  the intensity of the incident light, and  $\phi_f$  the photon flux of the incident radiation at temperature  $T_{bb}$ .  $\phi_f$  can either be described by the Planck's law for pure black-body radiation or taken as an input parameter for more realistic gray-body emitters or even selective emitters. Moreover,  $t_j^+$  is the internal transfer coefficient that relates the incident plane wave to the internal electric field propagating toward the positive  $x$ -direction in layer  $j$ , while  $\rho_j''$  and  $\delta_j''$  are the magnitude and argument of the internal complex reflection coefficient in layer  $j$ , respectively [41].

Using equation (3), the generation rate  $G_j(x)$  at an

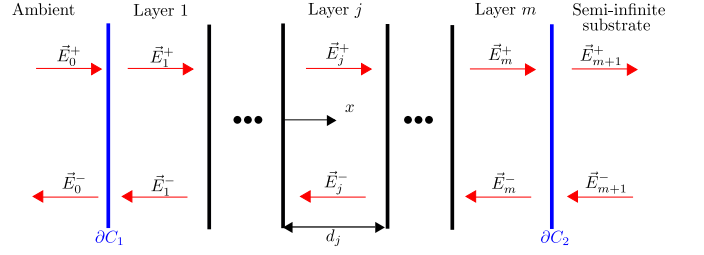


FIG. 2. Diagram of a multilayered structure having  $m$  layers between a semi-infinite transparent ambient and a semi-infinite substrate. The optical electric field in layer  $j$  is divided into the incident wave  $E_j^+$  and the reflected wave  $E_j^-$ . Each layer  $j$  is described by its thickness  $d_j$  and the complex refractive index  $\tilde{n}_j = n_j + ik_j$ .

arbitrary point  $x$  in layer  $j$  is derived:

$$G_j(x) = \int_E \frac{Q_j(x, E)}{E} dE, \quad E = \frac{hc}{\lambda}, \quad 0 \leq x \leq d_j \quad (4)$$

The coherence length  $L_c$  of a black-body radiation of temperature  $T_{bb}$  is given as [42]:

$$L_c = \frac{hc}{4kT_{bb}} \quad (5)$$

where  $k$  is the Boltzmann's constant. For the temperature range considered here (Fig. 1(c)),  $L_c$  is estimated to be significantly smaller compared to the thickness of the silicon substrate ( $\sim 500 \mu\text{m}$ ). For this reason, the use of ordinary OTMM will lead to narrow Fabry-Perot oscillations in the calculated reflectance, transmittance, and absorbance spectra. Thus, to account for the incoherency of light in the structure, the absorbance spectra  $\mathcal{A}(\lambda)$  was computed using the generalized transfer matrix method (GTMM), which is valid for mixed coherent/incoherent layer stacking [43]. Moreover, the model presented here considers the high injection regime as it is relevant to broader applications including concentrator TPV modules and laser power beaming.

### B. Numerical solution of the steady-state coupled Poisson drift-diffusion equations

The free carrier densities ( $n$ ,  $p$ ), involved in the system of equations (1), are estimated using the parabolic band approximation (PBA) and the Fermi-integral of index 1/2 ( $\mathcal{F}_{1/2}$ ) [52]. Moreover, the resolution of the Poisson equation using the Newton-Raphson method, involves the computation of the derivative of  $\mathcal{F}_{1/2}$  which is proportional to  $\mathcal{F}_{-1/2}$ . The numerical computation of the Fermi-integrals in a multilayered structure is a time-consuming and memory-intensive process. Here, we use an approximation of  $\mathcal{F}_j$  to simplify the calculation process

TABLE I. The physical parameters used in the simulation for the  $\text{Ge}_{0.83}\text{Sn}_{0.17}$   $p$ - $i$ - $n$  TPV cells

Material	Thickness (nm)		Energy (eV)			Effective masses ( $m_0$ ) [44]		Dielectric permittivity [45]	Mobility ( $\text{cm}^2/(\text{Vs})$ ) [46, 47]		Doping ( $\text{cm}^{-3}$ )		SRH lifetime ( $\mu\text{s}$ )		Auger coefficients ( $10^{-32} \text{ cm}^6/\text{s}$ )		Surface recombination velocity ( $\text{cm/s}$ ) [48]	
	$d$	$E_g$ [44]	$E_p$ [45]	$\chi_s$ [49]	$m_c$	$m_{hh}(m_{lh})$	$\epsilon_r$	$\mu_n$	$\mu_p$	$N_D$	$N_A$	$\tau_n = \tau_p$	$C_n$	$C_p$	$S_n$	$S_p$		
$p$ -layer	500							3895	421.43	0	$10^{18}$				$10^3$	$+\infty$		
$i$ -layer	2000	0.291	25.91	4	0.0243	0.0320 (0.0741)	17.36	3895	2505	0	0	2	3	7	*	*		
$n$ -layer	500							1888.2	2505	$10^{17}$	0		[50, 51]		$+\infty$	$10^3$		

Note: “\*” indicates that the parameter is not required.

[53]:

$$\mathcal{F}_{j-1}(y) = \left( \frac{j \cdot 2^j}{[b + y + (|y - b|^c + a^c)^{1/c}]^j} + \frac{e^{-y}}{\Gamma(j)} \right)^{-1} \quad (6)$$

where  $a = (1 + 3.75j + 0.025j^2)^{1/2}$ ,  $b = 1.19 + 0.61j$ ,  $c = 2(1 + (2 - \sqrt{2})2^{-j})$  and  $\Gamma$  is the Gamma function. More recent approaches have been presented in the literature for the computation of the Fermi integrals [54, 55]. However, this approximation has the merit to allow a simple calculation of the  $\mathcal{F}_j(y)$  for any real value of  $j$  and any  $y$  using only one expression and with acceptable accuracy.

A unique solution of Poisson’s equation requires the identification of the boundary conditions at the metal-semiconductor interfaces. Herein, different contact models are considered. An ideal ohmic contact is specified by assuming a vanishing electric field at the boundaries of the structure, and therefore, zero von Neumann boundary conditions. Schottky contacts are also established by employing Dirichlet boundary conditions for the electrostatic potential  $\phi$ . The latter depends on the work functions  $\phi_m$  of the metals, the voltage bias, the electron affinity  $\chi_s$  of the semiconductors, and the thermal equilibrium Fermi level.

In Si solar cells, the impact of the intrinsic recombination mechanisms (Auger and radiative recombination) on the conversion efficiency was shown to be negligible [56]. However for narrow-bandgap  $\text{Ge}_{1-y}\text{Sn}_y$  materials, depending on the material quality, these processes could become the most dominant. For that reason, the established formalism takes into account Auger, Shockley-Read-Hall (SRH), and radiative recombination mechanisms. The net non-radiative recombination rates are computed following the process described in [52]. As for the radiative recombination, rather than using the bimolecular recombination coefficient  $B$  to estimate the net rate, equation (7) below is used, where  $E_{f_n}$  and  $E_{f_p}$  are the quasi-Fermi levels,  $P$  is the Kane’s parameter,  $e$  is the elementary charge,  $n_r$  is the refractive index of the material,  $E_v^0 = E_v - e\phi - (\hbar^2/2m_v)k_{0,v}$ ,  $E_c^0 = E_c - e\phi + (\hbar^2/2m_c)k_{0,v}$ , with  $\phi$  the electrostatic potential, and  $f$  the Fermi-Dirac distribution [52]. Be-

sides,  $k_{0,v} = (2m_{c,v}^*/\hbar^2)^{1/2}\sqrt{\hbar\omega - E_c + E_v}$ , with  $m_{c,v}^*$  the reduced effective mass.

$$r_{\text{sp}}(\hbar\omega) = \left( \frac{P^2 n_r e^2 \hbar\omega}{6\pi^3 \hbar^4 c^3 \epsilon_0} \right) \sum_v \left( \frac{2m_{c,v}^*}{\hbar^2} \right) k_{0,v} \times f \left( \frac{E_c^0 - E_{f_n}}{k_B T} \right) f \left( \frac{E_{f_p} - E_v^0}{k_B T} \right) \quad (7)$$

$$R_{\text{rad}}(x) = \int_0^{+\infty} [r_{\text{sp}}(E, x) - r_{\text{sp}}^{\text{eq}}(E, x)] dE$$

This equation should be more general since the bimolecular recombination approximation is only accurate for non-degenerate materials where the quasi-Fermi levels are very close to the middle of the bandgap [57].

The drift-diffusion equation is solved numerically under different boundary conditions imposed on the quasi-Fermi levels at both electrical contacts. Indeed, at these boundaries, the values of the quasi-Fermi levels are mainly defined by the current density  $j_{n,p}$  and the surface recombination velocities  $S_{n,p}$  for electrons and holes at the contacts, as specified by equation (8), in which  $n_{eq}$  and  $p_{eq}$  are the carrier densities at thermal equilibrium [39].

$$\begin{aligned} j_n(\partial C_1) &= eS_{n,1} (n(\partial C_1) - n_{eq}(\partial C_1)) \\ j_n(\partial C_2) &= -eS_{n,2} (n(\partial C_2) - n_{eq}(\partial C_2)) \\ j_p(\partial C_1) &= -eS_{p,1} (p(\partial C_1) - p_{eq}(\partial C_1)) \\ j_p(\partial C_2) &= eS_{p,2} (p(\partial C_2) - p_{eq}(\partial C_2)) \end{aligned} \quad (8)$$

From these equations, the minority carriers that reach the surfaces  $\partial C_1$  and  $\partial C_2$  are supposed to recombine. However, for infinite values of surface recombination, the minority carrier density at the surface is defined by its thermal equilibrium value, and the quasi-Fermi level is therefore given by the thermal equilibrium Fermi level and the voltage bias applied. This situation is usually seen for  $p$ - $n$  junctions where the quasi-Fermi levels reach the same value at both ends of the structure [40, 58].

The system of coupled differential equations (1) is solved in a block-iterative way following the procedure described in [59]. This approach consists of alternating so-

lutions of Poisson's equation with fixed quasi-Fermi levels and the current equations with fixed electrostatic potential. The equations are repeatedly solved in each block until convergence is achieved before proceeding with the following outer iteration step in the other block. The  $J$ - $V$  characteristics of the TPV cell are extracted after solving (1) for different values of the voltage bias  $V$ . Afterward,  $V_{OC}$ ,  $J_{SC}$ , the fill factor (FF), and the PCE are computed. In this study, the PCE is defined as the ratio of the output electrical power to the incident power. However, to compare with data reported in the literature, the ratio of the output electrical power to the power absorbed by the device is also computed. This quantity is sometimes named the absorption efficiency ( $\eta_{abs}$ ) or the pairwise PCE, and it is appropriate for laboratory scale, experimental materials [60]. The physical parameters relevant to device simulations are summarized in Table I.

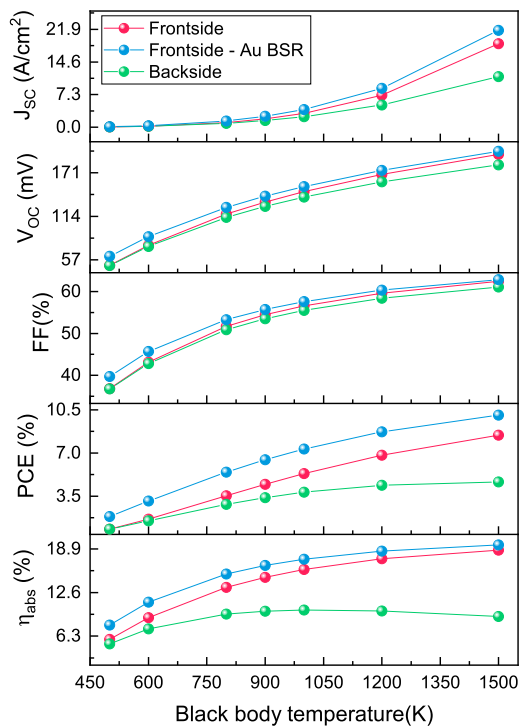


FIG. 3. Impact of the black-body temperature  $T_{bb}$  on the power conversion efficiency of the  $\text{Ge}_{0.83}\text{Sn}_{0.17}$   $p$ - $i$ - $n$  TPV.

### III. RESULTS AND DISCUSSION

The simulations are focused on  $\text{Ge}_{0.83}\text{Sn}_{0.17}$  heterostructures corresponding to a bandgap energy of 0.291 eV. The  $\text{Ge}_{0.83}\text{Sn}_{0.17}$ -based TPV cells, operating at 300 K, are illuminated by black-body radiation sources whose temperature  $T_{bb}$  is within the 500 K to 1500 K range.

Assuming ideal ohmic contacts, the evolution of the TPV electrical parameters with the radiation temperature is studied, for both front-side and back-side illuminations, and the results are presented in Fig. 3.

With the material parameters provided in Table I, the short-circuit current  $J_{SC}$  is mainly dominated by the absorption of the incident radiation and the generation rate. At a bandgap energy of  $\sim 0.291$  eV, only a small part of the black-body radiation emitted at 500 K is absorbed by the TPV cell, leading to relatively low values of generation rate and, therefore, a small  $J_{SC}$  of  $72.92 \text{ mA/cm}^2$  for front-side illumination. By increasing the temperature  $T_{bb}$ , the spectral radiant emittance of the source shifts to higher energies where more and more emitted photons are absorbed by the cell. In that situation, more EHPs are generated and collected in the  $p$ - $i$ - $n$  structure, contributing to the increase of the charge current, which reaches  $18.68 \text{ A/cm}^2$  at 1500 K.

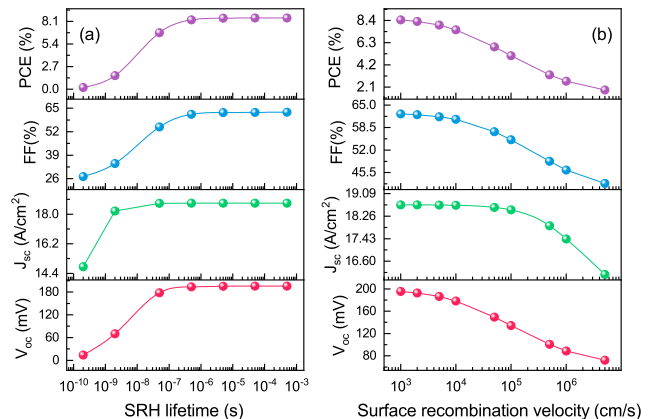


FIG. 4. Impact of the SRH lifetimes (a) and the surface trapping centers (b) on the key parameters of the  $\text{Ge}_{0.83}\text{Sn}_{0.17}$   $p$ - $i$ - $n$  TPV at  $T_{bb} = 1500$  K.

For an open circuit, no current flows across the device, and thus all the photo-generated charge carriers must recombine. Since the number of generated EHPs increases with the radiation temperature, the open-circuit recombination rate must be large enough to cancel out the generation rate and the current. For this to occur, the energy offset between the quasi-Fermi levels increases therefore leading to higher values of  $V_{OC}$ , as shown in the bottom panel of Fig. 3. Indeed,  $V_{OC}$  increases from 49.6 mV at 500 K to reach about 195 mV at 1500 K. At the same time, the maximum output power of the TPV cell increases with the source temperature, enabling significant improvements in the FF and the PCE. At 1500 K, for instance, a FF of  $\sim 62.5\%$  is estimated in addition to a PCE of about 8.5%. Starting from 1000 K, the difference between the TPV performance parameters under front-side and back-side illuminations starts to be noticeable. This difference can be explained by the higher number of EHPs generated in the  $i$ -layer when the radiation is sent to the top of the device. With the total recombination rate  $R(x)$  being negligible compared to  $G(x)$  at 0 V, more EHPs in the absorbing layer would lead to more current and thus to higher  $J_{SC}$ . For an open circuit, the increased number of EHPs will also lead to higher recombination

rates and higher voltage  $V_{OC}$ . The differences in these two parameters, combined with the maximum output electrical power  $P_m$ , induces the behavior observed for the FF, the PCE, and the absorption efficiency  $\eta_{abs}$ , even though the difference appears earlier around 600 K and is more pronounced for  $\eta_{abs}$ .

Besides, the concept of transmissive spectral control and its impact on the TPV efficiency is also investigated. Herein, a layer of gold is added at the bottom of the Si substrate to act as a back surface reflector (BSR) and mainly reflect radiation with energy lower than the  $\text{Ge}_{0.83}\text{Sn}_{0.17}$  bandgap, while absorbing radiation with higher energies [61]. The addition of this layer induces an increase of the sub-bandgap reflectance, with the average value going from  $\sim 50\%$  to  $\sim 80\%$ . At the same time, there is an increase of the absorption of radiation with higher energies, leading to the creation of more EHPs. However, only a slight overall improvement is observed, as shown in Fig. 3. Better improvements should be observed with the use of a more appropriate reflector (with a possible addition of a spacer) in our specific range of energy.

The impact of different material parameters on the performance of the GeSn-TPV device is also investigated. Herein, devices operating at 300 K with a black-body radiation at 1500 K are considered under the front-side illumination. At first, the SRH lifetimes  $\tau_n$  and  $\tau_p$  were varied between 200 ps and 1 ms to reveal the potential effect of growth defects on the TPV performance. For the sake of simplification and to reduce the number of parameters involved,  $\tau_n$  was assumed to be the same as  $\tau_p$ , and the obtained results are displayed in Fig. 4(a). For relatively small values of  $\tau_n$  and  $\tau_p$  (i.e., high defect density across the TPV structure), most of the photo-generated carriers are trapped by the defects inside the bandgap, resulting in a degradation of the performance as seen at 200 ps corresponding to a PCE of  $\sim 0.21\%$ . Expectedly, better performances are obtained as lifetimes increase. However, the performance saturates at a threshold around 1  $\mu\text{s}$  beyond which the increase in lifetime does not yield any meaningful improvement. From this value, the radiative recombination completely takes over the SRH recombination in the intrinsic layer, with a slight variation of the rate from one value of lifetime to the other, therefore explaining the saturation.

Moreover, using SRH lifetimes of 2  $\mu\text{s}$ , the impact of the quality of the interfaces at the metallic contacts on the TPV performance was investigated by varying the surface recombination velocities  $S_n$  of the  $p$ -layer and  $S_p$  of the  $n$ -layer from  $10^3$  to  $10^7$  cm/s. Here, again,  $S_n$  was assumed to be equal to  $S_p$  to simplify the analysis. High values of surface recombination velocity result from a high number of surface trapping centers per unit area in the border region and thus correspond to poor contact quality and degradation of the TPV performance, as shown in Fig. 4(b). In fact, the PCE decreases from  $\sim 8.45\%$  obtained at a surface recombination velocity of  $10^3$  cm/s to reach 1.83% at  $S_{n,p} = 5 \times 10^6$  cm/s. Similar behavior is also observed for the other parameters even though

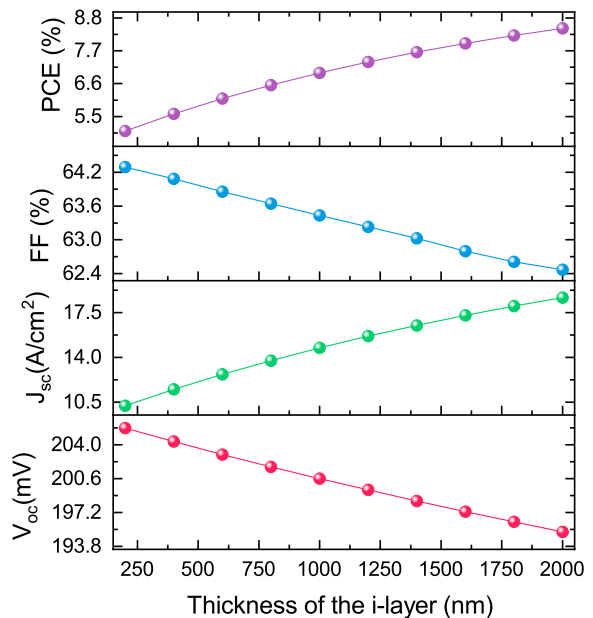


FIG. 5. Impact of the thickness of the  $i$ -layer upon the power conversion efficiency of the  $\text{Ge}_{0.83}\text{Sn}_{0.17}$   $p$ - $i$ - $n$  TPV.

$J_{SC}$  varies very slowly within this range of surface recombination velocities. This overall degradation indicates the significance of a good contact quality in achieving efficient TPV cells. The cell efficiency can be improved by passivating the surface to reduce the number of trapping centers and, at the same time, the recombination of the photo-generated carriers at the boundary regions [65].

The effect of the  $i$ -layer thickness ( $t_i$ ) on the performance of the TPV cell is crucial to both the overall absorption of the incident light and to the volume within which minority carriers can recombine. Using SRH lifetimes of 2  $\mu\text{s}$  and surface recombination velocities of  $10^3$  cm/s, the impact of the thickness of the  $i$ -layer on the TPV performance was investigated. Herein,  $t_i$  was varied from 200 to 2000 nm, and the obtained results are displayed in Fig. 5. The fraction of black body radiations absorbed by the TPV cell decreases when the thickness of the  $i$ -layer is reduced. In this case, fewer EHPs are generated, and  $J_{SC}$  is reduced, resulting in lower power density and lower PCE. The relative change is very small in the FF ( $\sim 3\%$  change) and  $V_{OC}$  (5%).

The investigated GeSn-based TPV cells are predicted to perform relatively well in comparison to compound semiconductors. For instance, under an incident power density  $P_{in}$  of  $3 \text{ W/cm}^2$  and at an emitter temperature of 1500 K, a PCE of 5.17% and an output power density  $P_{out}$  of  $154.97 \text{ mW/cm}^2$  are observed for GeSn-based devices. Under identical conditions, InAsSbP-based TPV cells deliver an efficiency of 0.66% and  $P_{out}$  of  $19.76 \text{ mW/cm}^2$ , as displayed in Table II. Similar behavior is also observed at lower values of  $P_{in}$ , where the GeSn-based device is shown to outperform both InAs- and GaInAsSbP-based devices (Table II). In addition to conventional  $p$ - $i$ - $n$  or  $p$ - $n$ - $n$  junction structures, the performance of narrow bandgap ICPV

TABLE II. Performance parameters of current narrow bandgap TPV cells.

Structure	Absorber material	$E_g$ (eV)	$T_c$ (K)	$P_{in}$ (W/cm <sup>2</sup> )	$J_{SC}$ (A/cm <sup>2</sup> )	$V_{OC}$ (V)	FF (%)	$\eta$ (%)	$P_{out}$ (mW/cm <sup>2</sup> )	Ref
<i>p-n-n</i>	InAs <sub>0.84</sub> Sb <sub>0.03</sub> P <sub>0.13</sub>	0.35	294	3	0.49	0.09	45.44	0.66	19.76	[62]
<i>p-n-n</i>	GaInAsSbP	0.35	300	0.5	0.29	0.03	33	0.53	2.66	[63]
<i>p-i-n</i>	InAs	0.35	300	0.32 0.72	0.21 0.89	0.02 0.06	28.09 37	0.33 3	1.05 21.6	[1] [18]
<i>p-i-n</i>	Ge <sub>0.83</sub> Sn <sub>0.17</sub> 2000 nm	0.29	300	0.3	0.21	0.08	42.95	2.24	6.67	This work
<i>p-i-n</i>	Ge <sub>0.83</sub> Sn <sub>0.17</sub> 2000 nm	0.29	300	3	2.08	0.14	54.96	5.17	154.97	This work
Superlattices <sup>a</sup>	InAs/GaSb 6 stages	0.22	300	17	3.58	0.35	35.41	2.59	440.74	[64]

<sup>a</sup> Unlike the other studies in which broadband sources were used to illuminate the devices, selective emitters (Interband cascade lasers) were used for the devices in the work in [64]

devices is also presented in Table II. These devices benefit from the type-II broken gap alignment at the InAs/GaSb interface, which mainly enables tunneling between different cascade stages in multi-stage devices. To mimic the characteristics of a selective emitter with a narrow emission spectrum, useful for reducing the thermalization and below-bandgap losses in a TPV system, a type-II interband cascade laser (ICL) with emission wavelengths near 4.3  $\mu\text{m}$  was employed to illuminate the different devices. In addition to reducing the losses, the ICL offers much higher incident power density compared to black body sources [20], leading therefore to more efficient ICPV with relatively high output power.

#### IV. CONCLUSION

This work presents an all-group IV mid-infrared thermophotovoltaic cell consisting of a fully relaxed GeSn double heterostructure with a bandgap energy of 0.29 eV. A new theoretical framework was introduced to evaluate the cell performance including an accurate description of the black-body radiation absorption and of the intrinsic recombination mechanisms. This study revealed that the GeSn cells can deliver efficiencies of up to 9%. A slight improvement is observed under the front side illumination but vanishes below 800 K. The use of a backside reflector was found to enhance cell efficiency. The impact of the material properties on the cell performance was also investigated in terms of the effects of thickness, SRH

lifetime, and surface recombination velocity. Although reducing the layer thickness from 2000 nm to 250 nm yields a relative decrease of less than 40% in the conversion efficiency, the latter is significantly more sensitive to SRH lifetimes and surface recombination velocity. In fact, a low lifetime has a detrimental impact on the heterostructure, thus hinting at the importance of achieving high material quality to exploit the full potential of GeSn cells. These silicon-integrated devices can be a cost-effective alternative to current narrow bandgap compound semiconductor technologies.

#### ACKNOWLEDGEMENTS

O.M. acknowledges support from NSERC Canada (Discovery, SPG, and CRD Grants), Canada Research Chairs, Canada Foundation for Innovation, Mitacs, PRIMA Québec, Defense Canada (Innovation for Defense Excellence and Security, IDEaS), the European Union's Horizon Europe research and innovation programme under grant agreement No 101070700 (MIRAQLS), and the US Army Research Office Grant No. W911NF-22-1-0277. R.S. acknowledges support from the United States AFOSR on grant FA9550-21-1-0347.

#### AUTHORS INFORMATION

Corresponding Authors:

\* [oussama.moutanabbir@polymtl.ca](mailto:oussama.moutanabbir@polymtl.ca)

Notes:

The authors declare no competing financial interest.

[1] Q. Lu, X. Zhou, A. Krysa, A. Marshall, P. Carrington, C.-H. Tan, and A. Krier, *Solar Energy Materials and Solar Cells* **179**, 334 (2018).

[2] W. R. Chan, V. Stelmakh, S. Karnani, C. M. Waits, M. Soljacic, J. D. Joannopoulos, and I. Celanovic, *Journal of Physics: Conference Series* **1052**, 012041 (2018).

- [3] X. Wang, R. Liang, P. Fisher, W. Chan, and J. Xu, *Journal of Propulsion and Power* **36**, 593 (2020).
- [4] L. Rizzo, J. F. Federici, S. Gatley, I. Gatley, J. L. Zunino, and K. J. Duncan, *Journal of Infrared, Millimeter, and Terahertz Waves* **41**, 979 (2020).
- [5] R. Q. Yang, W. Huang, and M. B. Santos, *Solar Energy Materials and Solar Cells* **238**, 111636 (2022).
- [6] I. Johnson, W. T. Choate, and A. Davidson, *Waste Heat Recovery. Technology and Opportunities in U.S. Industry*, Tech. Rep. (U.S. Department of Energy, 2008).
- [7] A. Thekdi and S. U. Nimbalkar, *Industrial Waste Heat Recovery - Potential Applications, Available Technologies and Crosscutting R&D Opportunities*, Tech. Rep. (U.S. Department of Energy, 2015).
- [8] M. Papapetrou and G. Kosmadakis, in *Salinity Gradient Heat Engines*, Woodhead Publishing Series in Energy, edited by A. Tamburini, A. Cipollina, and G. Micale (Woodhead Publishing, 2022) pp. 319–353.
- [9] M. M. A. Gamel, H. J. Lee, W. E. S. W. A. Rashid, P. J. Ker, L. K. Yau, M. A. Hannan, and M. Z. Jamaludin, *Materials* **14**, 4944 (2021).
- [10] G. P. Forcade, C. E. Valdivia, S. Molesky, S. Lu, A. W. Rodriguez, J. J. Krich, R. St-Gelais, and K. Hinzer, *Applied Physics Letters* **121**, 193903 (2022), <https://doi.org/10.1063/5.0116806>.
- [11] P. Mialhe, B. Affour, K. El-Hajj, and A. Khoury, *Active and Passive Electronic Components* **17**, 093424 (1900).
- [12] M. G. Mauk and V. M. Andreev, *Semiconductor Science and Technology* **18**, S191 (2003).
- [13] C. A. Wang, H. K. Choi, S. L. Ransom, G. W. Charache, L. R. Danielson, and D. M. DePoy, *Applied Physics Letters* **75**, 1305 (2003).
- [14] O. Sulima and A. Bett, *Solar Energy Materials and Solar Cells* **66**, 533 (2001).
- [15] T. Schlegl, in *AIP Conference Proceedings*, Vol. 738 (AIP, 2004) pp. 285–293.
- [16] M. Tan, L. Ji, Y. Wu, P. Dai, Q. Wang, K. Li, T. Yu, Y. Yu, S. Lu, and H. Yang, *Applied Physics Express* **7**, 096601 (2014).
- [17] M. M. A. Gamel, P. J. Ker, W. E. S. W. A. Rashid, H. J. Lee, M. A. Hannan, and M. Z. B. Jamaludin, *IEEE Access* **9**, 37091 (2021).
- [18] A. Krier, M. Yin, A. R. J. Marshall, M. Kesaria, S. E. Krier, S. McDougall, W. Meredith, A. D. Johnson, J. Inskip, and A. Scholes, *Infrared Physics & Technology* **73**, 126 (2015).
- [19] R. Q. Yang, Z. Tian, J. F. Klem, T. D. Mishima, M. B. Santos, and M. B. Johnson, *Applied Physics Letters* **96**, 063504 (2010).
- [20] R. T. Hinkey, Z.-B. Tian, S. M. S. S. Rassel, R. Q. Yang, J. F. Klem, and M. B. Johnson, *IEEE Journal of Photovoltaics* **3**, 745 (2013).
- [21] O. Moutanabbir, S. Assali, X. Gong, E. O'Reilly, C. A. Broderick, B. Marzban, J. Witzens, W. Du, S.-Q. Yu, A. Chelnokov, D. Buca, and D. Nam, *Applied Physics Letters* **118**, 110502 (2021).
- [22] M. R. M. Atalla, S. Assali, A. Attiaoui, C. Lemieux-Leduc, A. Kumar, S. Abdi, and O. Moutanabbir, *Advanced Functional Materials* **31**, 2006329 (2021).
- [23] M. R. M. Atalla, S. Assali, S. Koelling, A. Attiaoui, and O. Moutanabbir, *ACS Photonics* **9**, 1425 (2022).
- [24] D. Buca, A. Bjelajac, D. Spirito, O. Concepción, M. Gromovyi, E. Sakat, X. Lafosse, L. Ferlazzo, N. von den Driesch, Z. Ikonik, D. Grützmacher, G. Capellini, and M. El Kurdi, *Advanced Optical Materials* **10**, 2201024 (2022).
- [25] C.-Y. Chang, P.-L. Yeh, Y.-T. Jheng, L.-Y. Hsu, K.-C. Lee, H. Li, H. H. Cheng, and G.-E. Chang, *Photonics Research* **10**, 2278 (2022).
- [26] J. Chrétien, N. Pauc, F. Armand Pilon, M. Bertrand, Q.-M. Thai, L. Casiez, N. Bernier, H. Dansas, P. Gergaud, E. Delamadeleine, R. Khazaka, H. Sigg, J. Faist, A. Chelnokov, V. Reboud, J.-M. Hartmann, and V. Calvo, *ACS Photonics* **6**, 2462 (2019).
- [27] J. Chrétien, Q. M. Thai, M. Frauenrath, L. Casiez, A. Chelnokov, V. Reboud, J. M. Hartmann, M. El Kurdi, N. Pauc, and V. Calvo, *Applied Physics Letters* **120**, 051107 (2022).
- [28] A. Elbaz, D. Buca, N. von den Driesch, K. Pantzas, G. Patriarche, N. Zerounian, E. Herth, X. Checoury, S. Sauvage, I. Sagnes, A. Foti, R. Ossikovski, J.-M. Hartmann, F. Boeuf, Z. Ikonik, P. Boucaud, D. Grützmacher, and M. El Kurdi, *Nature Photonics* **14**, 375 (2020).
- [29] H.-J. Joo, Y. Kim, D. Burt, Y. Jung, L. Zhang, M. Chen, S. J. Parluhutan, D.-H. Kang, C. Lee, S. Assali, Z. Ikonik, O. Moutanabbir, Y.-H. Cho, C. S. Tan, and D. Nam, *Applied Physics Letters* **119**, 201101 (2021).
- [30] Y. Jung, D. Burt, L. Zhang, Y. Kim, H.-J. Joo, M. Chen, S. Assali, O. Moutanabbir, C. S. Tan, and D. Nam, *Photonics Research* **10**, 1332 (2022).
- [31] X. Li, L. Peng, Z. Liu, Z. Zhou, J. Zheng, C. Xue, Y. Zuo, B. Chen, and B. Cheng, *Photonics Research* **9**, 494 (2021).
- [32] X. Liu, J. Zheng, C. Niu, T. Liu, Q. Huang, M. Li, D. Zhang, Y. Pang, Z. Liu, Y. Zuo, and B. Cheng, *Photonics Research* **10**, 1567 (2022).
- [33] L. Luo, S. Assali, M. R. M. Atalla, S. Koelling, A. Attiaoui, G. Daligou, S. Martí, J. Arbiol, and O. Moutanabbir, *ACS Photonics* **9**, 914 (2022).
- [34] B. Marzban, L. Seidel, T. Liu, K. Wu, V. Kiyek, M. H. Zoellner, Z. Ikonik, J. Schulze, D. Grützmacher, G. Capellini, M. Oehme, J. Witzens, and D. Buca, *ACS Photonics*, acsphotronics.2c01508 (2022).
- [35] E. Talamas Simola, V. Kiyek, A. Ballabio, V. Schlykow, J. Frigerio, C. Zucchetti, A. De Iacovo, L. Colace, Y. Yamamoto, G. Capellini, D. Grützmacher, D. Buca, and G. Isella, *ACS Photonics* **8**, 2166 (2021).
- [36] H. Tran, T. Pham, J. Margetis, Y. Zhou, W. Dou, P. C. Grant, J. M. Grant, S. Al-Kabi, G. Sun, R. A. Soref, J. Tolle, Y.-H. Zhang, W. Du, B. Li, M. Mortazavi, and S.-Q. Yu, *ACS Photonics* **6**, 2807 (2019).
- [37] S. Xu, W. Wang, Y.-C. Huang, Y. Dong, S. Masudy-Panah, H. Wang, X. Gong, and Y.-C. Yeo, *Optics Express* **27**, 5798 (2019).
- [38] Y. Zhou, Y. Miao, S. Ojo, H. Tran, G. Abernathy, J. M. Grant, S. Amoah, G. Salamo, W. Du, J. Liu, J. Margetis, J. Tolle, Y.-h. Zhang, G. Sun, R. A. Soref, B. Li, and S.-Q. Yu, *Optica* **7**, 924 (2020).
- [39] J. Nelson, *The Physics of Solar Cells* (Imperial College Press, 2003).
- [40] S. M. Sze and K. K. Ng, *Physics of Semiconductor Devices*, 3rd ed. (Wiley-Interscience, 2007).
- [41] L. A. A. Pettersson, L. S. Roman, and O. Inganäs, *Journal of Applied Physics* **86**, 487 (1999).
- [42] A. Donges, *European Journal of Physics* **19**, 245 (1998).
- [43] C. C. Katsidis and D. I. Siapkas, *Appl. Opt.* **41**, 3978 (2002).
- [44] S. Assali, A. Dijkstra, A. Attiaoui, E. Bouthillier, J. Haverkort, and O. Moutanabbir, *Physical Review Ap-*

- plied **15**, 024031 (2021).
- [45] G.-E. Chang, S.-w. Chang, and S. L. Chuang, *IEEE Journal of Quantum Electronics* **46**, 1813 (2010).
- [46] M. Bosi and G. Attolini, *Progress in Crystal Growth and Characterization of Materials* **56**, 146 (2010).
- [47] D. Caughey and R. Thomas, *Proceedings of the IEEE* **55**, 2192 (1967).
- [48] M. Virgilio, C. L. Manganelli, G. Grosso, T. Schroeder, and G. Capellini, *Journal of Applied Physics* **114**, 243102 (2013).
- [49] Ioffe, Basic parameters at 300 k, <http://www.ioffe.ru/SVA/NSM/Semicond/Ge/basic.html>.
- [50] R. Conradt and J. Aengenheister, *Solid State Communications* **10**, 321 (1972).
- [51] S. Marchetti, M. Martinelli, R. Simili, M. Giorgi, and R. Fantoni, *Physica Scripta* **64**, 509 (2001).
- [52] S. L. Chuang, *Physics of Photonic Devices*, 2nd ed., Wiley Series in Pure and Applied Optics (Wiley, 2009).
- [53] X. Aymerich-Humet, F. Serra-Mestres, and J. Millan, *Journal of Applied Physics* **54**, 2850 (1983).
- [54] I. I. Guseinov and B. A. Mamedov, *Chinese Physics B* **19**, 050501 (2010).
- [55] T. Fukushima, *Applied Mathematics and Computation* **234**, 417 (2014).
- [56] A. Richter, M. Hermle, and S. W. Glunz, *IEEE Journal of Photovoltaics* **3**, 1184 (2013).
- [57] G. Daligou, A. Attiaoui, S. Assali, P. Del Vecchio, and O. Moutanabbir, *Radiative carrier lifetime in  $ge_{1-x}sn_x$  mid-infrared emitters* (2023).
- [58] B. Streetman and S. Banerjee, *Solid State Electronic Devices*, Prentice Hall series in solid state physical electronics (Prentice Hall, 2000).
- [59] S. Hackenbuchner, *Elektronische Struktur von Halbleiternanobauelementen im thermodynamischen Nichtgleichgewicht*, 1st ed., Ausgewählte Probleme der Halbleiterphysik und Technologie No. 48 (Walter-Schottky-Inst, 2002).
- [60] T. Burger, C. Sempere, B. Roy-Layinde, and A. Lenert, *Joule* **4**, 1660 (2020).
- [61] B. Wernsman, R. Siergiej, S. Link, R. Mahorter, M. Palmisiano, R. Wehrer, R. Schultz, G. Schmuck, R. Messham, S. Murray, C. Murray, F. Newman, D. Taylor, D. DePoy, and T. Rahmlow, *IEEE Transactions on Electron Devices* **51**, 512 (2004).
- [62] M. Mauk, O. Sulima, J. Cox, and R. Mueller, in *Proceedings of 3rd World Conference on Photovoltaic Energy Conversion, 2003*, Vol. 1 (2003) pp. 224–227 Vol.1.
- [63] K. J. Cheetham, P. J. Carrington, N. B. Cook, and A. Krier, *Solar Energy Materials and Solar Cells* **95**, 534 (2011).
- [64] W. Huang, J. A. Massengale, Y. Lin, L. Li, R. Q. Yang, T. D. Mishima, and M. B. Santos, *Journal of Physics D: Applied Physics* **53**, 175104 (2020).
- [65] S. Bose, J. M. V. Cunha, S. Suresh, J. De Wild, T. S. Lopes, J. R. S. Barbosa, R. Silva, J. Borme, P. A. Fernandes, B. Vermang, and P. M. P. Salomé, *Solar RRL* **2**, 1800212 (2018).